

Ballistic magnon circulators with magnetic skyrmions

Haichuan Zhang(张海川), Hongbin Wu(武宏斌), and Jin Lan(兰金)
Citation: Chin. Phys. B, 2025, 34 (**10**): 107503. DOI: 10.1088/1674-1056/addaa6
http://cpb.iphy.ac.cn; http://iopscience.iop.org/cpb

What follows is a list of articles you may be interested in

Magnon behavior in YIG film under microwave excitation investigated by Brillouin light scattering

Guofu Xu(徐国服), Kang An(安康), Wenjun Ma(马文俊), Xiling Li(李喜玲), C. K. Ong, Chi Zhang(张驰), and Guozhi Chai(柴国志)
Chin. Phys. B, 2025, 34 (**6**): 067507. DOI: 10.1088/1674-1056/add24c

Orbital magnetic field effect on spin waves in a triangular lattice tetrahedral antiferromagnetic insulator

Pi-Ye Zhou(周丕烨), Xiao-Hui Li(李晓慧), and Yuan Wan(万源)
Chin. Phys. B, 2025, 34 (**6**): 067501. DOI: 10.1088/1674-1056/adca1f

Strain-manipulated dispersion characteristics of magnonic crystals with Dzyaloshinskii-Moriya interaction and applications on spin-wave devices

Chuhan Zhou(周楚涵), Xiaotian Jiao(焦晓天), Jiaxi Xu(徐佳熙), Zhaonian Jin(金兆年), Lin Chen(陈琳), and Zhikuo Tao(陶志阔)
Chin. Phys. B, 2025, 34 (**2**): 027501. DOI: 10.1088/1674-1056/ad9892

Skyrmion motion induced by spin-waves on magnetic nanotubes

Tijjani Abdulrazak, Xuejuan Liu(刘雪娟), Zhenyu Wang(王振宇), Yunshan Cao(曹云姗), and Peng Yan(严鹏)
Chin. Phys. B, 2024, 33 (**10**): 107504. DOI: 10.1088/1674-1056/ad5d64

Consistency between domain wall oscillation modes and spin wave modes in nanostrips

Xinwei Dong(董新伟) and Zhenjiang Wu(吴振江)
Chin. Phys. B, 2024, 33 (**6**): 067502. DOI: 10.1088/1674-1056/ad2a6b

---

SPECIAL TOPIC — Advanced magnonics

Ballistic magnon circulators with magnetic skyrmions

Haichuan Zhang(张海川)[1,2], Hongbin Wu(武宏斌)[1,2], and Jin Lan(兰金)[1,2,†]

[1] *Center for Joint Quantum Studies and Department of Physics, School of Science, Tianjin University, Tianjin* 300072, *China*
[2] *Tianjin Key Laboratory of Low Dimensional Materials Physics and Preparing Technology, Tianjin University, Tianjin* 300354, *China*

(Received 16 April 2025; revised manuscript received 14 May 2025; accepted manuscript online 20 May 2025)

Spin waves, quantized as magnons, constitute a fundamental class of excitations and serve as one of the primary angular momentum carriers in magnetic systems. Devoid of Joule heating, a magnonic device that routes spin waves between different ports holds promise for an energy-efficient information infrastructure. Here, we systematically investigate the transport behavior of a magnetic skyrmion-based magnon circulator, a representative device that directs spin wave flow in a non-reciprocal manner. Particularly, a ballistic transport model is established, where the scattering of spin waves by magnetic skyrmions is simplified as magnon deflection by fictitious electromagnetic fields within the skyrmions. Through the combination of ballistic analyses and micromagnetic simulations, the circulation performance is rigorously evaluated for multiple magnon circulators.

Keywords: spin wave, ballistic transport, magnetic skyrmion, circulator

PACS: 75.30.Ds, 73.23.Ad, 85.70.–w, 42.25.Ja

DOI: 10.1088/1674-1056/addaa6 **CSTR:** 32038.14.CPB.addaa6

1. Introduction

As an alternative spin carrier to spin-polarized electrons, spin waves (quantized as magnons) extend the concepts of spintronics from magnetic metals and semiconductors to insulators.[1,2] Moreover, via the common magnetic nature, the dynamic spin wave interacts intimately with the static magnetic configurations,[3–5] hence is intrinsically compatible with well-established magnetic storage technologies.[6,7] Developing magnonic devices that harness and exploit spin waves is vital for unleashing the full potential of magnetic systems.[8–10]

Stimulated by the rapid developments of experimental techniques to excite and detect spin waves,[11–15] diverse designs of magnonic devices have attracted considerable attention in recent years.[10] By introducing additional phase, several types of spin wave interferometers have been realized through the application of Oersted fields[16,17] or electric fields,[18] the deposition of magnetic impurities,[19] and the placement of magnetic domain walls.[20] Through polarization-dependent scattering, elementary devices such as spin wave polarizers, retarders, and rotators have been designed.[21–25] By constraining the propagation direction through bound states, total reflection, or edge states, devices such as spin wave diodes,[3] spin wave fibers,[26,27] and splitters[28] have been proposed. Moreover, utilizing the intrinsic nonlinearity, magnon transistors,[29] repeaters,[30] as well as frequency combs[31] and frequency multipliers[32,33] have initiated intriguing paradigms for advanced functionalities. To concentrate on the physical disciplines, most current designs predominantly rely on (quasi-) one-dimensional magnetic wires or stripes, or simply employ open boundaries.

Similar to its electronic counterpart,[34,35] a magnonic device with multiple ports provides significantly richer functionalities and greater flexibility, at the cost of increased geometric complexity. To handle the considerable geometric complications, theoretical investigations on multiple-port magnonic devices are typically conducted via micromagnetic simulations.[36–39] An alternative approach with much lower computational cost is to track the ballistic trajectories of magnons,[40] where the spin wave packet acts as an intermediate bridge. Equipped with magnon kinetics, the interactions between magnons and magnetic domain walls,[41] skyrmions,[40,42–44] bimerons,[45] and hopfions[46] can be studied efficiently and elegantly, albeit under open boundary conditions. The full integration of ballistic trajectories into multi-port magnonic devices, akin to their electronic counterparts, still awaits systematic development.

In this work, we investigate the ballistic transport behavior of three-port magnon circulators with different geometric shapes and magnetic configurations, in both ferromagnetic and antiferromagnetic environments. With the aid of magnon trajectories across fictitious electromagnetic fields induced by geometric boundaries and magnetic configurations, the circulation functionalities are analyzed in a fast yet quantitative manner. Furthermore, in an antiferromagnetic platform, the circulation direction becomes interlocked with the spin wave

[†]Corresponding author. E-mail: lanjin@tju.edu.cn

© 2025 Chinese Physical Society and IOP Publishing Ltd. All rights, including for text and data mining, AI training, and similar technologies, are reserved.

polarization via the intimate interplay between magnetization topology and precession. The ballistic magnons, rather than coherent spin waves, provide an alternative perspective for understanding and designing magnonic devices.

The remainder of this work is organized as follows. In Section 2, a ballistic transport model for a magnetic-texture-based magnon device is established by transforming spin wave scattering into magnon deflection. In Section 3, the ballistic transport behavior of magnon circulators is analyzed through the combination of magnon trajectories and spin wave fluxes. In Section 4, the polarization-dependent behavior in a magnon circulator built upon a synthetic antiferromagnetic film is demonstrated. A brief conclusion is provided in Section 5.

2. Basic model

2.1. Spin wave dynamics upon a magnetic texture

We consider a ferromagnetic film extending in the x–y plane, where the magnetization direction is denoted by a unit vector $\boldsymbol{m}$. The magnetic dynamics is governed by the Landau–Lifshitz–Gilbert (LLG) equation

$$\dot{\boldsymbol{m}} = -\gamma \boldsymbol{m} \times \boldsymbol{h} + \alpha \boldsymbol{m} \times \dot{\boldsymbol{m}}, \tag{1}$$

where $\dot{\boldsymbol{m}} \equiv \partial_t \boldsymbol{m}$, γ is the gyromagnetic ratio, and α is the Gilbert damping constant. The effective magnetic field is $\boldsymbol{h} = 2/(\mu_0 M_\mathrm{s})[A\nabla^2 \boldsymbol{m} + K\boldsymbol{m}\cdot\hat{\boldsymbol{z}} - D\hat{\boldsymbol{z}} \times (\nabla \times \boldsymbol{m})]$, where A is the exchange coupling constant, K is the easy-axis anisotropy along $\hat{\boldsymbol{z}}$, and D is the interfacial-type Dzyaloshinskii–Moriya (DM) interaction strength. The dipolar interaction is not included explicitly, since for the exchange-type spin waves of interest, its main effect is to renormalize the magnetic anisotropy from $K \to K - \mu_0 M_\mathrm{s}/2$.

The total magnetization $\boldsymbol{m}$ in LLG Eq. (1) can be naturally decomposed into the static magnetic texture part $\boldsymbol{m}_0$ and the dynamic spin wave part $\delta\boldsymbol{m}$: $\boldsymbol{m} = \boldsymbol{m}_0 + \delta\boldsymbol{m}$. Due to the unity constraint $|\boldsymbol{m}| = |\boldsymbol{m}_0| = 1$, the transverse condition $\boldsymbol{m}_0 \cdot \delta\boldsymbol{m} = 0$ is satisfied everywhere in the small-amplitude limit $|\delta\boldsymbol{m}| \ll 1$. By introducing a local frame $\hat{\boldsymbol{e}}_{r/\theta/\phi}$ aligned with the texture magnetization, with $\hat{\boldsymbol{e}}_r \equiv \boldsymbol{m}_0$, the spin wave is described by $\delta\boldsymbol{m} = m_\theta \hat{\boldsymbol{e}}_\theta + m_\phi \hat{\boldsymbol{e}}_\phi$, which can also be expressed in complex form as $\psi = m_\theta - \mathrm{i} m_\phi$.

In the presence of a magnetic texture, the spin wave dynamics can generally be recast from LLG Eq. (1) into a Schrödinger-like equation[3,40,47]

$$\mathrm{i}\dot{\psi} = \frac{2\gamma}{\mu_0 M_\mathrm{s}}[A(-\mathrm{i}\nabla + \boldsymbol{a})^2 + K]\psi, \tag{2}$$

where $\boldsymbol{a}$ is the fictitious vector potential induced by inhomogeneous texture magnetizations. The fictitious vector potential consists of two parts $\boldsymbol{a} = \boldsymbol{a}_0 + \boldsymbol{a}_D$, where $\boldsymbol{a}_0 = (\hat{\boldsymbol{z}} \times \boldsymbol{m}_0)/(1 + \boldsymbol{m}_0 \cdot \hat{\boldsymbol{z}})$ is induced by the magnetic topology, and $\boldsymbol{a}_D = (D/2A)\hat{\boldsymbol{z}} \times \boldsymbol{m}_0$ arises from the DM interaction.

In the short-wavelength limit, the local dispersion relation corresponding to Eq. (2) is given by

$$\omega = \frac{2\gamma}{\mu_0 M_\mathrm{s}}(A\boldsymbol{k}^2 + K), \tag{3}$$

where $\hbar\boldsymbol{k} = \hbar(\boldsymbol{q} + \boldsymbol{a})$ is the canonical momentum, and ω and $\boldsymbol{q}$ are the local frequency and wavevector, respectively.

2.2. Magnon kinetics upon fictitious magnetic fields

In the spirit of the eikonal approximation,[48] the spin wave dynamics in Eq. (2) can be transformed into magnon dynamics by treating the local dispersion in Eq. (3) as a Hamiltonian in the phase space $(\boldsymbol{r}, \boldsymbol{k})$. More explicitly, the magnon dynamics is governed by

$$\dot{\boldsymbol{r}} = \frac{\partial \omega}{\partial \boldsymbol{k}} = \frac{4\gamma A}{\mu_0 M_\mathrm{s}}\boldsymbol{k}, \tag{4a}$$

$$\dot{\boldsymbol{k}} = -\frac{\partial \omega}{\partial \boldsymbol{r}} = -\frac{4\gamma A q_0}{\mu_0 M_\mathrm{s}}\boldsymbol{k} \times \boldsymbol{b}, \tag{4b}$$

where $\dot{\boldsymbol{r}} = \boldsymbol{v}$ is the magnon velocity, q_0 is the elementary charge, and $\boldsymbol{b} = (1/q_0)\nabla \times \boldsymbol{a}$ is the fictitious magnetic field. Equation (4a) establishes the correspondence between the magnon velocity and the spin wave group velocity; Eq. (4b) indicates that the magnon is subject to a Lorentz-like force, and thus its canonical momentum $\boldsymbol{k}$ changes only its direction while keeping its magnitude constant.

The combination of Eqs. (4a) and (4b) yields the simplified kinetics of magnons[41]

$$m_\mathrm{sw}\ddot{\boldsymbol{r}} = -q_0 \dot{\boldsymbol{r}} \times \boldsymbol{b}, \tag{5}$$

where $m_\mathrm{sw} = \hbar k/|\dot{\boldsymbol{r}}| = \hbar\mu_0 M_\mathrm{s}/(4\gamma A)$ is the effective magnon mass. For magnons traveling in the x–y plane, only the z-component of the fictitious magnetic field is relevant, $\boldsymbol{b} = b\hat{\boldsymbol{z}}$. Following the convention of the vector potential $\boldsymbol{a}$, the fictitious magnetic field $b = b_0 + b_D$ is given by[40,49]

$$b_0 = \frac{1}{q_0}\boldsymbol{m}_0 \cdot \left(\frac{\partial \boldsymbol{m}_0}{\partial x} \times \frac{\partial \boldsymbol{m}_0}{\partial y}\right), \tag{6a}$$

$$b_D = \frac{1}{q_0}\frac{D}{2A}\nabla \cdot \boldsymbol{m}_0, \tag{6b}$$

which are directly determined by the texture magnetization $\boldsymbol{m}_0$.

2.3. Ballistic transport in a magnonic device

We consider a magnonic device consisting of several ports and a central scattering region, where the spin wave is directed between the peripheral ports through control in the central region. Typically, each terminal is regarded as a semi-infinite waveguide for spin waves, and the central scattering

arises from both geometric constrictions and magnetic impurities. The transport properties of a magnon device are described by

$$I_p^- = S_{pq} I_q^+, \tag{7}$$

where p,q denote the terminal indices, $I_p^{\pm}$ is the in/out spin wave flux, and S_{pq} is the scattering matrix.

Instead of dealing with the intricate spin-wave dynamics governed by Eq. (2), an effective alternative is to analyze magnon trajectories directly. To account for reflections caused by the boundaries, the magnon kinetics in Eq. (5) is modified to

$$m_{\rm sw}\ddot{\boldsymbol{r}} = -q_0\left(\boldsymbol{e} + \dot{\boldsymbol{r}} \times \boldsymbol{b}\right), \tag{8}$$

where $\boldsymbol{e}$ represents an artificial electric field applied along the normal direction of the thin boundary layer, designed to achieve specular reflection of magnons at boundaries. This field acts like a high potential barrier at the boundary for wave reflection, and both mechanisms serve to confine magnons within the material by preventing transmission across the interface. By setting the magnon velocity according to Eq. (4a) and the magnon number via the spin wave intensity $n = |\psi|^2/\hbar$, the ballistic magnon transport is then investigated by weighting magnon trajectories determined by Eq. (8).

3. Ballistic magnon circulators

3.1. Concepts and setups

A circulator, a non-reciprocal device that transports signals along a single cyclic direction, is one of the fundamental components in information processing.[50–52] Particularly, the scattering matrix of an ideal three-port circulator is given by

$$\begin{pmatrix} I_1^- \\ I_2^- \\ I_3^- \end{pmatrix} = \begin{pmatrix} 0 & 0 & 1 \\ 1 & 0 & 0 \\ 0 & 1 & 0 \end{pmatrix} \begin{pmatrix} I_1^+ \\ I_2^+ \\ I_3^+ \end{pmatrix}, \tag{9}$$

where the circulating order is $1 \to 2 \to 3 \to 1$.

Unlike other approaches that rely on dipolar interactions,[37–39] the magnon circulator in this work is realized by depositing magnetic skyrmions in the central magnetic region, where the non-reciprocity arises from the nontrivial magnetic topology.[36] Owing to the magnetic nature of both spin waves and skyrmions, the device operates purely magnetically.

To quantitatively investigate the transport properties of a magnon circulator, two complementary computational approaches are employed: (i) micromagnetic simulations (via Mumax3[53]) by solving LLG Eq. (1); (ii) ballistic calculations by solving the magnon kinetic Eq. (8). The magnetic parameters are as follows: the saturation magnetization $M_{\rm s} = 1.94 \times 10^3$ A/m, the exchange coupling constant $A = 4 \times 10^{-14}$ J/m, the easy-axis anisotropy $K = 47$ J/m^3, the DM strength $D = 1.22 \times 10^{-6}$ J/m^2, and the damping constant $\alpha = 1 \times 10^{-5}$. Skyrmions are first stabilized through relaxation, and their magnetization profiles are used to generate the fictitious magnetic field via Eq. (6). The fictitious magnetic field, together with the artificial electric field, is then used as input to the magnon kinetic Eq. (8).

3.2. Circulator with one magnetic skyrmion

We consider one of the simplest three-port magnon circulators, a ring-shaped circulator shown in Fig. 1(a), where a magnetic skyrmion is placed in the central region. The skyrmion motion is neglected in this work since only small-amplitude spin waves are used in the micromagnetic simulations, and it can be further pinned through interface or surface engineering.[54] An antenna is located at port 1 to excite spin waves, and an absorption layer is set at the end of each port to suppress unwanted reflections. The spin wave scattering between different ports is then collected by monitoring signals entering these absorption layers.

The fictitious magnetic field corresponding to the relaxed magnetization profile in Fig. 1(a) is plotted in Fig. 1(b), via the translation of Eq. (6). The entire fictitious magnetic field is oriented outward, resulting from the combined contributions of b_0 induced by magnetic topology and b_D induced by DM interaction. When a bulk-type Dzyaloshinskii–Moriya (DM) interaction is present instead of an interfacial-type, the mathematical form of the fictitious field in Eq. (6b) changes to $b_D = (D/2Aq_0)[(\nabla \times \boldsymbol{m}_0) \cdot \hat{\boldsymbol{z}}]$. However, the spatial profile remains unchanged, as the skyrmion configuration transforms correspondingly from a Néel-type to a Bloch-type configuration. In addition, an electric field of strength 9×10^3 V/m is artificially applied at the boundary along the inward normal direction within a layer 50 nm thick (10 nm inside and 40 nm outside the device region), as schematically depicted in Fig. 1(c).

Since the magnon velocity increases while the Hall angle decreases for higher spin wave frequencies (see Appendix A), the frequency $f = 35$ GHz is chosen as a trade-off between deflection magnitude and response time. Correspondingly, magnons are launched from port 1 with a velocity $v = 2475$ m/s and mass $m_{\rm sw} = 7.2 \times 10^{-30}$ kg. They undergo repeated deflections by the skyrmion and reflections at the boundaries before ultimately exiting through one of the three ports (see supplementary video 1 for time evolutions of scattering processes). Because of clockwise deflections, a majority of the magnons enter port 2, while only a minority reach port 3 or are reflected back into port 1, resulting in an anticlockwise circulation pattern. The magnon trajectories agree well with the spin wave flux profiles extracted from micromagnetic simulations in Fig. 1(e), confirming effective circulating

operations in the ballistic regime.

Moreover, the scattering coefficient S_{p1} with $p = \{1,2,3\}$ extracted from both micromagnetic simulations and ballistic trajectories is plotted in Fig. 1(f), showing strong agreement. In a wide frequency range from 20 GHz to 65 GHz, the transmission probability from port 1 to port 2 dominates, as indicated by $S_{21} \gg S_{11} > S_{31}$. The deviation from an ideal circulator in Eq. (9) with $S_{21} = 1$ is mainly caused by the insufficient bending of magnon trajectories across the skyrmion, as shown in Fig. 1(e). At elevated spin wave frequencies, the desired transmission coefficient S_{21} diminishes, while the parasitic transmission S_{31} increases, primarily due to the weakened deflection efficacy of the skyrmion.

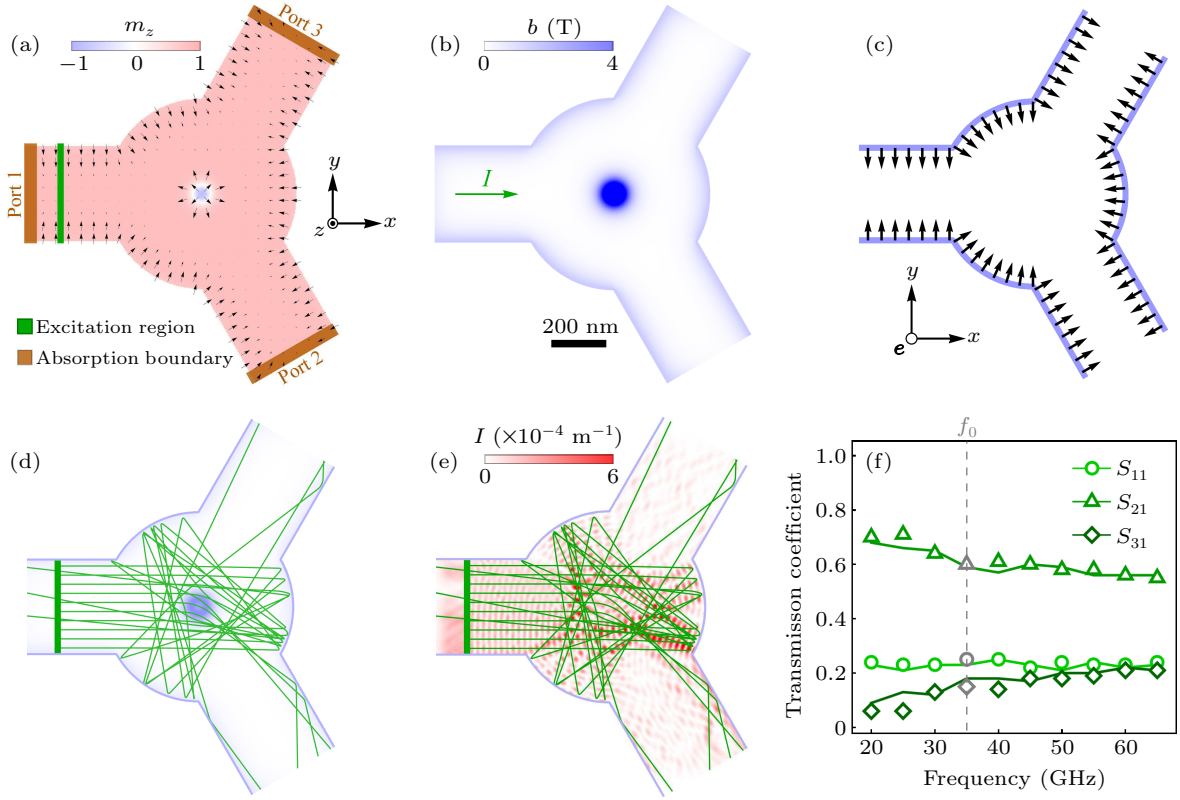


Fig. 1. Magnon circulator with one magnetic skyrmion. (a) Schematics of a magnon circulator. The arrows indicate the in-plane magnetization components, while the color represents the out-of-plane component. (b) Fictitious magnetic field b induced by inhomogeneous magnetizations. (c) Artificial electric fields $\boldsymbol{e}$ applied at the boundary. (d) Magnon trajectories within the circulator, calculated from Eq. (8). (e) Spin wave fluxes within the circulator, extracted from micromagnetic simulations of the LLG equation (1). The background color encodes the magnitude of spin wave fluxes. The spin wave frequency is set to $f_0 = 35$ GHz. (f) Scattering coefficient S_{p1} as a function of spin wave frequency. The dots are extracted from micromagnetic simulations, and the lines are based on the ballistic calculations. The gray dashed line highlights the corresponding scattering coefficients in panel (e).

3.3. Circulators with three magnetic skyrmions

To improve the circulating efficiency, three magnetic skyrmions are prepared inside the circulator to enhance the bending of magnon trajectories, as illustrated in Fig. 2(a). Corresponding to each magnetic skyrmion, a copy of the fictitious magnetic field is imprinted into the central scattering region. As a result of the subsequent deflections, mainly provided by the two fictitious magnetic fields near port 1 and port 2, most magnons are directly guided into port 2; at the same time, after multiple reflections, a small fraction of magnons leak into port 1 and port 3. The main features of the above ballistic magnon trajectories are confirmed by the spin-wave flux profile extracted from micromagnetic simulations in Fig. 2(b).

As shown in Fig. 2(c), the port 1-to-port 2 transmission coefficient S_{21} reaches approximately 0.85 across the frequency range of 20 GHz to 65 GHz, exhibiting a marked enhancement in the high-frequency regime compared with the one-skyrmion configuration in Fig. 1(f). This improvement is mainly attributed to the cumulative magnon deflection provided by the two additional magnetic skyrmions. Meanwhile, the reflection S_{11} back to port 1 remains non-negligible, primarily due to magnons that cannot directly enter port 2 even after undergoing two successive deflections. The major obstacle arises from the bottleneck at port 2 with abrupt corners, which reflects magnons backward when they are incident nearly perpendicularly to the boundary.

To alleviate this bottleneck effect, a modified triangular-shaped magnon circulator is proposed, as depicted in Fig. 2(d), where smoother boundaries are constructed along the opposite sides of the three ports. Guided by reflections at the input boundary, most magnons experience one or two deflections by

the magnetic skyrmions and smoothly enter port 2, as demonstrated in Fig. 2(e) (see also supplementary video 2 for the time evolution of the scattering process). This scenario is further corroborated by the spin-wave flux profile extracted from micromagnetic simulations, which reveals the formation of a distinct transmission channel between ports 1 and 2, along with a characteristic flow-confluence pattern emerging near the entrance of port 2.

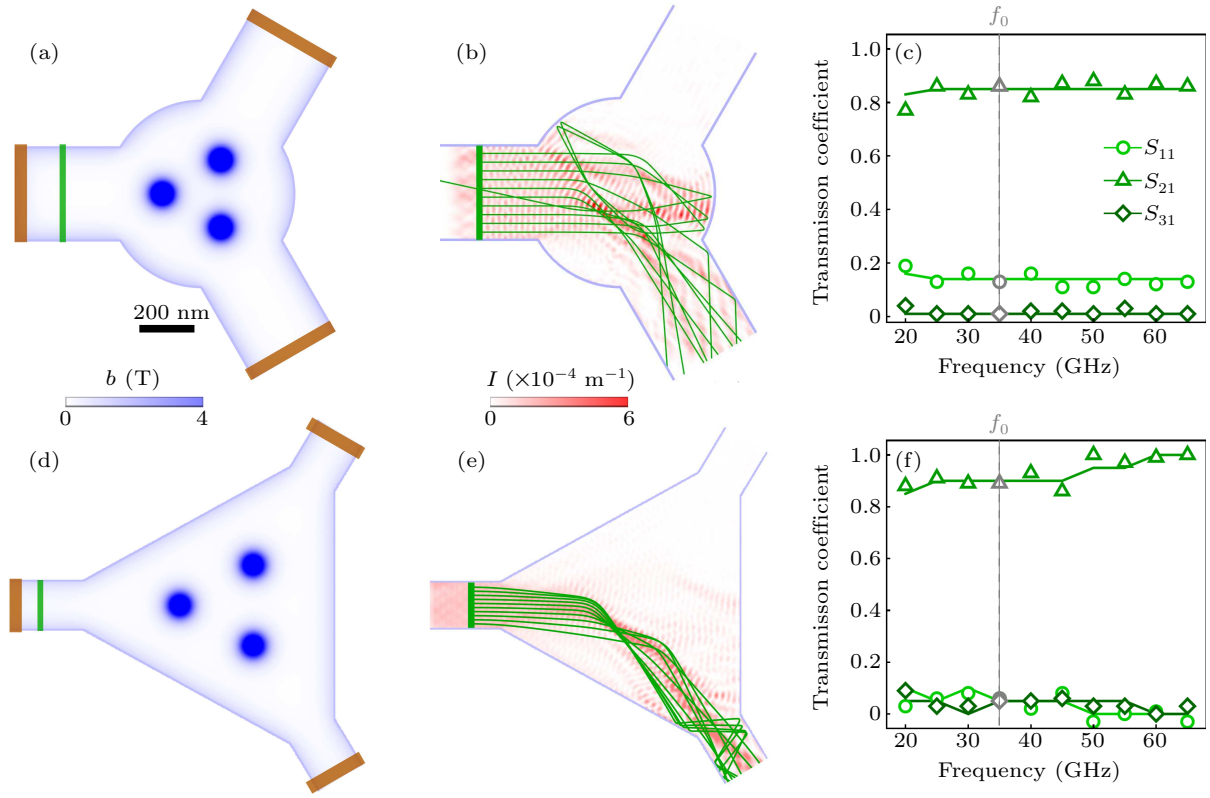


Fig. 2. Magnon circulators of ring shape (a)–(c) and triangular shape (d)–(f) with three magnetic skyrmions. (a) and (d) Geometric setup and the corresponding fictitious magnetic field. (b) and (e) Magnon trajectories from ballistic calculations and spin wave fluxes from micromagnetic simulations. The spin wave frequency is $f_0 = 35$ GHz. (c) and (f) Scattering coefficients S_{p1} as a function of spin wave frequency. Figure elements follow the conventions of Fig. 1.

The shape optimization yields exceptional circulating performance, with the port 1-to-port 2 transmission exceeding $S_{21} > 0.9$, while the undesired port 1-to-port 3 transmission and the port 1-to-port 1 reflection are markedly suppressed, with $S_{31} \approx S_{11} < 0.1$, as shown in Fig. 2(f). The enhancement of S_{21} at elevated frequencies arises from the cumulative deflection provided by multiple skyrmions. Compared to the ring-shaped configuration in Fig. 2(c), the triangular-shaped geometry achieves an average increase of 0.1 in S_{21}, demonstrating a significant performance improvement enabled by eliminating the geometric bottlenecks. Therefore, the device geometry provides an additional means to achieve comprehensive control over ballistic magnon transport, complementing traditional strategies based on magnetic configurations.

4. Polarization-dependent ballistic magnon circulator

The magnon circulator implementations demonstrated above can be directly adapted from ferromagnetic to antiferromagnetic systems. By fully leveraging the polarization degree of freedom, antiferromagnetic platforms enable the design of chiral circulators that couple spin wave polarization to specific circulation directions, a mechanism detailed in the subsequent analysis.

4.1. Antiferromagnetic dynamics

Consider a synthetic antiferromagnetic film extending in the x–y plane, which consists of two ferromagnetic sublayers coupled antiferromagnetically.[55] Denoting the magnetizations in the upper and lower layers as $\boldsymbol{m}_1$ and $\boldsymbol{m}_2$, respectively, the coupled LLG equation is described by

$$\dot{\boldsymbol{m}}_j = -\gamma \boldsymbol{m}_j \times \boldsymbol{h}_j + \alpha \boldsymbol{m}_j \times \dot{\boldsymbol{m}}_j, \tag{10}$$

where $j = 1, 2$ denotes the sublayer index. The effective magnetic field acting on $\boldsymbol{m}_j$ is $\boldsymbol{h}_j = \frac{2}{\mu_0 M_s}\left[A\nabla^2 \boldsymbol{m}_j + K m_j^z \hat{\boldsymbol{z}} - D(\nabla \times \boldsymbol{m}_j) - J\boldsymbol{m}_{\bar{j}}\right]$, where $\bar{j}$ denotes the complementary layer index ($\bar{1} = 2$ and $\bar{2} = 1$), and J is the interlayer exchange coupling constant.

Due to the antiferromagnetic coupling J in Eq. (10), the magnetic texture develops with the two sublayer magnetizations aligned antiparallel to each other, denoted by $\boldsymbol{m}_1 =$

$-\boldsymbol{m}_2 = \boldsymbol{n}_0$. Upon the staggered magnetization $\boldsymbol{n}_0$, a local frame $\hat{\boldsymbol{e}}_{r/\theta/\phi}$ is attached with $\hat{\boldsymbol{e}}_r \equiv \boldsymbol{n}_0$, and the spin wave is described by $\delta\boldsymbol{m}_j = m_j^\theta \hat{\boldsymbol{e}}_\theta + m_j^\phi \hat{\boldsymbol{e}}_\phi$. In complex form, the spin wave is rewritten as $\psi_j^\sigma = m_j^\theta - \mathrm{i}\sigma m_j^\phi$, where $\sigma = \pm 1$ represents the right- and left-circular polarizations. With the above denotations, the spin wave dynamics is recast from Eq. (10) into coupled Schrödinger-like equations,[21]

$$\mathrm{i}\sigma\chi\dot{\psi}_j^\sigma = \frac{2\gamma}{\mu_0 M_\mathrm{s}}\left[A(-\mathrm{i}\nabla + \sigma\boldsymbol{a})^2 + K + J\right]\psi_j^\sigma + J\psi_{\bar{j}}^\sigma, \quad (11)$$

where $\chi = (-1)^{j+1}$ takes opposite signs for sublayers $j = 1, 2$, and $\boldsymbol{a}$ is the vector potential defined in Eq. (2). In the short-wavelength limit, the local dispersion degenerates into two circular modes with

$$\omega = \frac{2\gamma}{\mu_0 M_\mathrm{s}}\sqrt{(Ak^2 + K + 2J)(Ak^2 + K)}, \quad (12)$$

where $\hbar\boldsymbol{k} = \hbar(\boldsymbol{q} + \sigma\boldsymbol{a})$ is the canonical momentum.

Following a similar procedure as for Eq. (8), the spin wave dynamics in Eq. (11) is transformed into magnon kinetics

$$m_\mathrm{sw}\ddot{\boldsymbol{r}} = -q_0(\boldsymbol{e} + \sigma\dot{\boldsymbol{r}} \times \boldsymbol{b}), \quad (13)$$

where $\boldsymbol{b}$ is the fictitious magnetic field in Eq. (6), and $\boldsymbol{e}$ is the fictitious electric field artificially set at the boundary. The magnon velocity is $\boldsymbol{v} = \partial\omega/\partial\boldsymbol{k} = 8\gamma^2 A\boldsymbol{k}(Ak^2 + K + J)/(\mu_0^2 M_\mathrm{s}^2\omega)$, and the magnon mass is $m_\mathrm{sw} = \hbar\boldsymbol{k}/\boldsymbol{v} = \mu_0^2 M_\mathrm{s}^2\hbar\omega/[8\gamma^2 A(Ak^2 + K + J)]$. Magnons in Eq. (13) are deflected in opposite directions for opposite magnon spins $\sigma = \pm 1$, reflecting the intrinsic connection between magnetic texture topology and spin wave polarization.

4.2. Polarization-dependent circulator

Similar to the setup in Fig. 2(d), a triangle-shaped circulator with three magnetic skyrmions is placed in a synthetic antiferromagnetic film with interlayer coupling $J = 609$ J/m^3, as depicted in Fig. 3(a). For a spin wave frequency $f = 50$ GHz, a column of magnons is launched from port 1 with velocity $v = 2640$ m/s and mass $m_\mathrm{sw} = 6.8 \times 10^{-30}$ kg. According to Eq. (13), magnons with spin $\sigma = \pm 1$ are deflected clockwise and anticlockwise by the fictitious magnetic field, and are collected at ports 2 and 3, respectively.

The polarization-dependent circulating functionality is corroborated by the spin wave flux profile obtained from micromagnetic simulations in Fig. 3(b). A linearly polarized spin wave, composed of equal contributions from left- and right-circular modes, is injected into port 1. As the wave propagates through the three skyrmions in the central region, the right-circular modes are deflected downward to port 2, while the left-circular modes are directed upward to port 3 (see Supplementary video 3 for time evolutions of scattering processes). Furthermore, the scattering coefficients collected from both ballistic calculations and micromagnetic simulations in Fig. 3(c) demonstrate that nearly all magnons are channeled into their designated ports, with only minimal leakage observed.

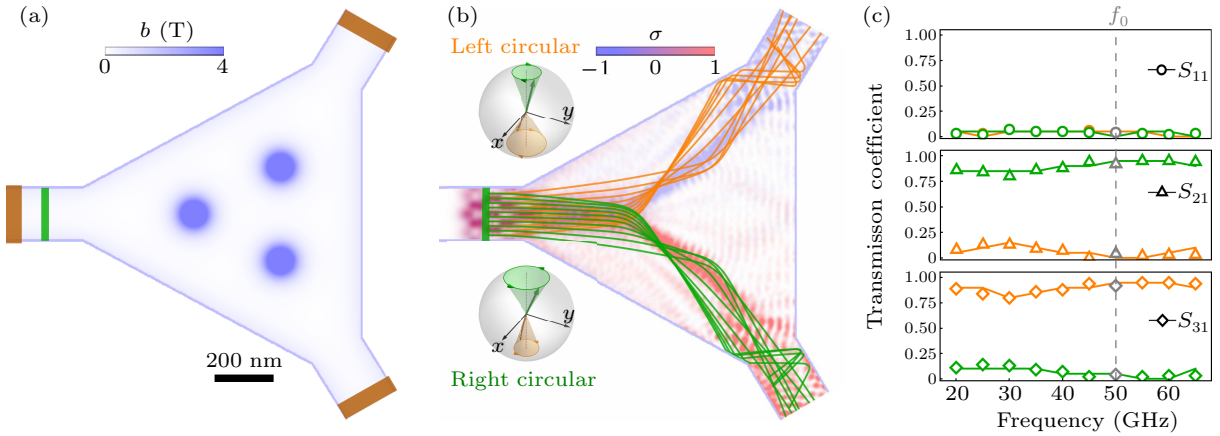


Fig. 3. Polarization-dependent magnon circulator upon an antiferromagnetic film. (a) Geometric setup and the corresponding fictitious magnetic field. (b) Magnon trajectories from ballistic calculations and spin wave fluxes from micromagnetic simulations. The spin wave frequency is $f_0 = 50$ GHz. Orange and green lines correspond to magnons with spin $\sigma = \pm 1$, and the blue/red/purple background colors encode the spin wave fluxes for left-circular, right-circular, and linear polarizations, respectively. (c) Scattering coefficient S_{p1} as a function of spin wave frequency. Figure elements follow the conventions of Fig. 1.

5. Conclusion

In conclusion, designs of magnon circulators in both ferromagnetic and antiferromagnetic environments are systematically investigated using a combination of ballistic modeling and micromagnetic simulations. Optimizing magnon trajectories through controlled skyrmion reconfiguration and geometric engineering enables the device to achieve exceptional circulation efficiency. The interplay between spin wave propagation and magnon trajectories provides a new paradigm for designing functional magnonic devices.

Appendix A: Magnon Hall angle

The magnon deflection by a magnetic skyrmion is characterized by the magnon Hall angle,[56,57] as depicted in Fig. A1. From the magnetization distribution in a magnetic skyrmion in Fig. A1(a), the fictitious magnetic field profile is derived via Eq. (6) and plotted in Fig. A1(b). Based on magnon kinetics in Eq. (5), the magnon trajectories starting from a column of magnons on the left side and penetrating through the fictitious magnetic field are collected, which overlap well with the spin wave fluxes obtained from micromagnetic simulations in Fig. A1(c).

The magnon Hall angle φ obtained from the ballistic trajectories is plotted in Fig. A1(d), which agrees well with the theoretical estimation based on the magnetic topology,[58]

$$\varphi = \arctan\left(\frac{4\pi}{5kR}\right), \tag{A1}$$

where k is the wavevector and R is the size of the magnetic skyrmion. With increasing spin wave frequency f (and wavevector k), the magnon Hall angle φ decreases monotonically, due to the increase of the normalized wavevector kR.

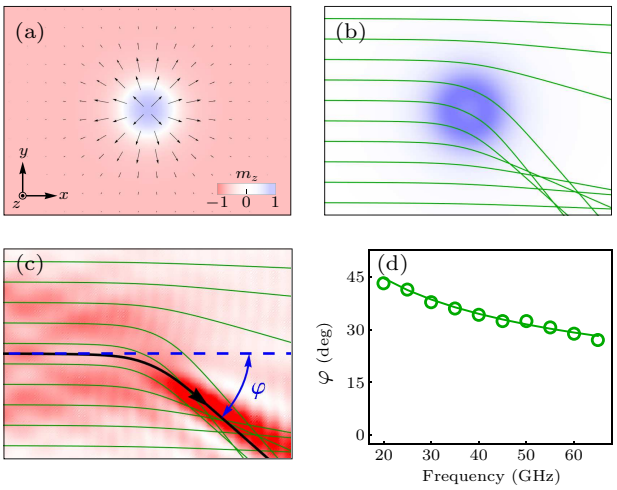


Fig. A1. The magnon Hall angle. (a) Schematic of a magnetic skyrmion. Arrows represent the in-plane magnetization component $m_x\hat{\boldsymbol{x}} + m_y\hat{\boldsymbol{y}}$, and the color encodes the out-of-plane component m_z. (b) Magnon trajectories across a magnetic skyrmion. (c) Spin wave flux profile extracted from micromagnetic simulations. (d) Magnon Hall angle as a function of spin wave frequency. Dots are extracted from ballistic trajectories in panel (b), and the solid line is obtained from the theoretical equation (A1).

Acknowledgments

This work was supported by the National Natural Science Foundation of China (Grant Nos. 12374117 and 11904260) and the Natural Science Foundation of Tianjin (Grant No. 20JCQNJC02020).

References

[1] Cornelissen L J, Liu J, Duine R A, Youssef J B and van Wees B J 2015 *Nat. Phys.* **11** 1022
[2] Lebrun R, Ross A, Bender S A, Qaiumzadeh A, Baldrati L, Cramer J, Brataas A, Duine R A and Kläui M 2018 *Nature* **561** 222
[3] Lan J, Yu W, Wu R and Xiao J 2015 *Phys. Rev. X* **5** 041049
[4] Han J, Zhang P, Hou J T, Siddiqui S A and Liu L 2019 *Science* **366** 1121
[5] Yu W, Lan J and Xiao J 2020 *Phys. Rev. Appl.* **13** 024055
[6] Parkin S S P, Hayashi M and Thomas L 2008 *Science* **320** 190
[7] Fert A, Cros V and Sampaio J 2013 *Nat. Nanotechnol.* **8** 152
[8] Chumak A V, Vasyuchka V I, Serga A A and Hillebrands B 2015 *Nat. Phys.* **11** 453
[9] Yu H, Xiao J and Schultheiss H 2021 *Phys. Rep.* **905** 1
[10] Flebus B, Grundler D, Rana B, *et al.* 2024 *J. Phys.: Condens. Matter* **36** 363501
[11] Wang Q, Verba R, Heinz B, Schneider M, Wojewoda O, Davídková K, Levchenko K, Dubs C, Mauser N J, Urbánek M, Pirro P and Chumak A V 2023 *Sci. Adv.* **9** eadg4609
[12] Girardi D, Finizio S, Donnelly C, Rubini G, Mayr S, Levati V, Cuccurullo S, Maspero F, Raabe J, Petti D and Albisetti E 2024 *Nat. Commun.* **15** 3057
[13] Zhang Y, Qiu L, Chen J, Wu S, Wang H, Malik IA, Cai M, Wu M, Gao P, Hua C, Yu W, Xiao J, Jiang Y, Yu H, Shen K and Zhang J 2025 *Nat. Mater.* **24** 69
[14] Liu C, Ai F, Reisbick S, Zong A, Pofelski A, Han MG, Camino F, Jing C, Lomakin V and Zhu Y 2025 *Nat. Mater.* **24** 406
[15] Lan G, Liu K Y, Wang Z, Xia F, Xu H, Guo T, Zhang Y, He B, Li J, Wan C, Bauer G E W, Yan P, Liu G Q, Pan X Y, Han X and Yu G 2025 *Nat. Commun.* **16** 1178
[16] Schneider T, Serga A A, Leven B, Hillebrands B, Stamps R L and Kostylev M P 2008 *Appl. Phys. Lett.* **92** 022505
[17] Rousseau O, Rana B, Anami R, Yamada M, Miura K, Ogawa S and Otani Y 2015 *Sci. Rep.* **5** 09873
[18] Liu T and Vignale G 2011 *Phys. Rev. Lett.* **106** 247203
[19] Dobrovolskiy O V, Sachser R, Bunyaev S A, Navas D, Bevz V M, Zelent M, Śmigaj W, Rychły J, Krawczyk M, Vovk R V, Huth M and Kakazei G N 2019 *ACS Appl. Mater. Interfaces* **11** 17654
[20] Hertel R, Wulfhekel W and Kirschner J 2004 *Phys. Rev. Lett.* **93** 257202
[21] Lan J, Yu W and Xiao J 2017 *Nat. Commun.* **8** 178
[22] Faridi E, Kim S K and Vignale G 2022 *Phys. Rev. B* **106** 094411
[23] Ye F and Lan J 2021 *Phys. Rev. B* **104** L180401
[24] Wu H and Lan J 2022 *Phys. Rev. B* **105** 174427
[25] Liu Y and Lan J 2023 *Phys. Rev. B* **108** L180407
[26] Yu W, Lan J, Wu R and Xiao J 2016 *Phys. Rev. B* **94** 140410
[27] Xing X and Zhou Y 2016 *NPG Asia Mater.* **8** e246
[28] Wang X S, Zhang H W and Wang X R 2018 *Phys. Rev. Appl.* **9** 024029
[29] Chumak A V, Serga A A and Hillebrands B 2014 *Nat. Commun.* **5** 4700
[30] Wang Q, Verba R, Davídková K, Heinz B, Tian S, Rao Y, Guo M, Guo X, Dubs C, Pirro P and Chumak A V 2024 *Nat. Commun.* **15** 7577
[31] Wang Z, Yuan H Y, Cao Y, Li Z X, Duine R A and Yan P 2021 *Phys. Rev. Lett.* **127** 037202
[32] Koerner C, Dreyer R, Wagener M, Liebing N, Bauer H G and Woltersdorf G 2022 *Science* **375** 1165
[33] Leenders R A, Afanasiev D, Kimel A V and Mikhaylovskiy R V 2024 *Nature* **630** 335
[34] Datta S 1995 *Electronic Transport in Mesoscopic Systems* (Cambridge: Cambridge University Press)
[35] Ferry D K, Goodnick S M and Bird J 2009 *Transport in Nanostructures* (Cambridge: Cambridge University Press)
[36] Daniels M W, Yu W, Cheng R, Xiao J and Xiao D 2019 *Phys. Rev. B* **99** 224433
[37] Szulc K 2020 *Phys. Rev. Appl.* **14** 034063
[38] Wang Q, Chumak A V and Pirro P 2021 *Nat. Commun.* **12** 2636
[39] Zhao J, Feng L, Ma M and Ma F 2023 *J. Magn. Magn. Mater.* **586** 171161
[40] Lan J and Xiao J 2021 *Phys. Rev. B* **103** 054428
[41] Lan J, Yu W and Xiao J 2021 *Phys. Rev. B* **103** 214407
[42] Jin Z, Yao X, Wang Z, Yuan HY, Zeng Z, Wang W, Cao Y and Yan P 2023 *Phys. Rev. Lett.* **131** 166704
[43] Zhang X, Ezawa M, Xiao D, Zhao GP, Liu Y and Zhou Y 2015 *Nanotechnology* **26** 225701
[44] Zhang X, Müller J, Xia J, Garst M, Liu X and Zhou Y 2017 *New J. Phys.* **19** 065001
[45] Liang X, Lan J, Zhao G, Zelent M, Krawczyk M and Zhou Y 2023 *Phys. Rev. B* **108** 184407

[46] Zhang Z, Lin K, Zhang Y, Bournel A, Xia K, Kläui M and Zhao W 2023 *Sci. Adv.* **9** eade7439
[47] van Hoogdalem KA, Tserkovnyak Y and Loss D 2013 *Phys. Rev. B* **87** 024402
[48] Landau L and Lifshitz E 1990 *The Classical Theory of Fields* No. 2 in Course of Theoretical Physics (Beijing: World Publishing Corporation)
[49] Kim S K, Nakata K, Loss D and Tserkovnyak Y 2019 *Phys. Rev. Lett.* **122** 057204
[50] Fleury R, Sounas DL, Sieck CF, Haberman MR and Alù A 2014 *Science* **343** 516
[51] Rasmussen C, Quan L and Alù A 2021 *J. Appl. Phys.* **129** 210903
[52] Song C, Zhao L, Liu J and Jiang W 2022 *Nano Lett.* **22** 9638
[53] Vansteenkiste A, Leliaert J, Dvornik M, Helsen M, Garcia-Sanchez F and Van Waeyenberge B 2014 *AIP Adv.* **4** 107133
[54] Ohara K, Zhang X, Chen Y, Wei Z, Ma Y, Xia J, Zhou Y and Liu X 2021 *Nano Lett.* **21** 4320
[55] Duine R A, Lee K J, Parkin S S P and Stiles M D 2018 *Nat. Phys.* **14** 217
[56] Schütte C and Garst M 2014 *Phys. Rev. B* **90** 094423
[57] Iwasaki J, Beekman A J and Nagaosa N 2014 *Phys. Rev. B* **89** 064412
[58] Wu H and Lan J 2025 *Phys. Rev. B* **112** 064410